

## Article

# The Effect of Fit Clearance between Outer Race and Housing on Vibration Characteristics of a Cylindrical Roller Bearing with Localized Defects

Fengtao Wang <sup>1</sup>, Xin Ling <sup>1</sup>, Zhen Zhang <sup>1</sup> , Peng Dai <sup>1</sup> , Shuping Yan <sup>2,\*</sup> and Lei Wang <sup>1</sup>

<sup>1</sup> School of Mechanical Engineering, Anhui Polytechnic University, Wuhu 241000, China; wangfengt1985@163.com (F.W.); lingxin9899@163.com (X.L.); zhangzhen@ahpu.edu.cn (Z.Z.); daipeng\_ahpu@163.com (P.D.); wangdalei2000@126.com (L.W.)

<sup>2</sup> Anhui Key Laboratory of High-Performance Non-Ferrous Metal Materials, Wuhu 241000, China

\* Correspondence: ysp620@163.com

**Abstract:** Due to bolt looseness or operating ambient temperature, fit clearance can often be found between the outer ring and housing. The vibration characteristics of a cylindrical roller bearing with localized defects are greatly affected by the fit clearance and the accuracy of bearing fault diagnosis may be reduced. Thus, a mathematical model for a cylindrical roller bearing was constructed and the interaction between the outer ring and housing was described. The classical localized defects were modeled, such as the inner ring defect, outer ring defect and roller defect. The relative experiments were conducted to check the constructed model. Then, it was found that the RMS (Root Mean Square) of housing acceleration decreased with increasing housing stiffness and viscous damping. When the fit clearance and friction coefficient increased, the RMS values increased. Except for housing stiffness and viscous damping, there were no uniform change rules of defect frequency amplitudes for other conditions. In the bearing with an outer ring defect or roller defect, the shock times of housing acceleration and the contact force between outer ring and housing were delayed, while fit clearance decreased. However, contrary variation trends were found for the inner ring defect. If the phase difference between defect location and rotor unbalanced force increased, the RMS and acceleration fluctuation amplitudes for the inner ring defect decreased. When the location angle of the outer ring defect increased, RMS and frequency amplitudes increased and  $RMS_y/RMS$  decreased. The calculated results may provide the theoretical foundation for condition monitoring rotating machinery systems.

**Keywords:** vibration characteristics; cylindrical roller bearing; fit clearance; localized defects; housing



**Citation:** Wang, F.; Ling, X.; Zhang, Z.; Dai, P.; Yan, S.; Wang, L. The Effect of Fit Clearance between Outer Race and Housing on Vibration Characteristics of a Cylindrical Roller Bearing with Localized Defects.

*Machines* **2022**, *10*, 415.

<https://doi.org/10.3390/machines10060415>

[machines10060415](https://doi.org/10.3390/machines10060415)

Academic Editors: Te Han, Ruonan Liu, Zhibin Zhao and Pradeep Kundu

Received: 23 April 2022

Accepted: 23 May 2022

Published: 25 May 2022

**Publisher's Note:** MDPI stays neutral with regard to jurisdictional claims in published maps and institutional affiliations.



**Copyright:** © 2022 by the authors. Licensee MDPI, Basel, Switzerland. This article is an open access article distributed under the terms and conditions of the Creative Commons Attribution (CC BY) license (<https://creativecommons.org/licenses/by/4.0/>).

## 1. Introduction

In view of their superior performance, cylindrical roller bearings are often used as one of the key parts in various machineries. The bearings are expected to have a longer life. However, due to the heavy loads, high working temperature and other factors, lubrication conditions in the bearing become poor. Then, excessive wear can occur, and electrostatic sensing is used to treat this early failure [1]. Later, a crack below the surface occurs and propagates, and localized defects are incurred [2]. The localized defects may lead to serious safety incidents, and the fault diagnosis method must be used for detecting the defects [3].

Current fault diagnosis methods are mainly based on vibration accelerations, and a number of studies on the vibration mechanism of cylindrical roller bearings with localized defects have been conducted. Shao et al. [4] proposed a vibration model for cylindrical roller bearing with localized defects. In this model, time-varying deflection and no-Hertzian contact stiffness were considered, and the ring defects were described by the half-sine function. Then, with the help of the simplified Gupta's model, a dynamic model for the defective cylindrical roller bearing was developed by Wang et al. [5], and the effects of defect sizes

on the bearing vibration characteristics were discussed. On the basis of the finite element method, the influence of defect edge discontinuities on the bearing vibration characteristics was investigated by Liu et al. [6]. Later, the following improvements were made: the non-Hertzian interaction between the logarithmic roller and ring was calculated [7], the rotor-housing-roller bearing system was reconstructed [8], the defect zone was described according to the roughness surface based on the Greenwood and Williamson method [9] and the model for defect extensions was built [10]. Using the energy approach, the defective bearing model was developed by Patel et al. [11,12] and the non-linear dynamic behaviors of the defective bearing were investigated. The contact model for describing defect geometry was proposed by Liu et al. [13]. Tang et al. [14] used the Gupta method and finite element method to discuss the influence of defect sizes and loads on stress in the defect zone. The defective bearing model with roller skew and roller title was developed by Patel et al. [15,16]. On the basis of the spring-mass-damping model, chaotic performances of the defective bearing system were investigated by Patra et al. [17]. In virtue of Gupta's model, Niu et al. [18] and Cao et al. [19,20] studied the performances of the bearing with roller defect, multiple defects and waviness. A model for the flexible bearing with defects was proposed by Xu et al. [21], with which the effects of the flexible structure on the bearing defect signatures were investigated.

In the aforementioned studies, the outer ring was often fixed to housing. However, due to bolt looseness or the operating ambient temperature, fit clearance between outer raceway and housing occurred [22,23]. The bearing vibration characteristics are affected significantly [24], which is less considered by researchers. Thus, following Gupta's method, an effective model for cylindrical roller bearing is proposed in this study, there are defects on the surface of inner ring, outer ring and roller. The interaction between outer ring and housing is described. Then, the effects of fit clearance and its related factors on the vibration characteristics of cylindrical roller bearing are investigated in detail, such as housing stiffness, the friction coefficient and viscous damping. The research results help to configure suggestions for the fault diagnosis of cylindrical roller bearings.

## 2. Model of a Defective Cylindrical Roller Bearing with Fit Clearance between Outer Race and Housing

A cylindrical roller bearing model with localized defects was built, and the outer ring-housing fit clearance was taken into account. Then, some necessary assumptions were made, such as: the housing is fixed, the cage is not considered, other bearing components only have planar motions, there are only elasticity deformations in the contact zones, the lubrication is adequate, and the change of temperature is ignored. In order to make the descriptions succinct, the interaction between outer ring and housing is detailed, other factors are introduced and more details can be obtained in Ref. [5].

### 2.1. Interaction between a Roller and Rings

In this section, the interaction between a roller and outer ring is detailed to obtain the force and moment on the roller, inner ring and outer ring. Firstly, it was necessary to confirm the related frames and spatial vectors. In Figure 1, the inertial frame  $OXYZ$ , roller center  $B$ , outer ring center  $R$  are represented. Fully crown geometry is always apparent when decreasing the edge contact stress between a roller and rings [25]. Thus, the slice method must be used for the roller and the contact point  $P$  between a roller slice and the outer ring is provided. Next, the vector from contact point  $P$  to the outer ring center  $R$  is:

$$\mathbf{r}_{pr} = \mathbf{r}_{pb} + \mathbf{r}_b - \mathbf{r}_r \quad (1)$$

where,  $\mathbf{r}_b$  is the position vector of the roller center,  $\mathbf{r}_r$  is the position vector of the ring center,  $\mathbf{r}_{pb}$  is the vector from the contact point to the roller center. Then, the overlap between the roller slice and the outer ring is:

$$\delta = \mathbf{r}_{pr3} - 0.5d_r \quad (2)$$

where, 3 is the third part of the vector  $\mathbf{r}_{pr}$ ,  $d_r$  denotes the raceway diameter. The contact force is given as:

$$Q = k_r \delta^{10/9} \quad (3)$$

where,  $k_r$  is the Hertzian line contact stiffness coefficient. Following which the tractive force is given as:

$$f = \mu Q \quad (4)$$

where,  $\mu$  is the tractive coefficient based on the relative sliding speed vector between a roller and outer ring, and the formula is:

$$\mathbf{v}_{br} = \mathbf{v}_r + \boldsymbol{\omega}_r \times \mathbf{r}_{pr} - \mathbf{v}_b - \boldsymbol{\omega}_b \times \mathbf{r}_{pb} \quad (5)$$

where,  $\mathbf{v}_r$  and  $\boldsymbol{\omega}_r$  are the movement speed vector and rotate speed vector of the outer ring,  $\mathbf{v}_b$  and  $\boldsymbol{\omega}_b$  are the movement speed vector and rotate speed vector of the roller. Then, the sum force and torque vectors on the roller and ring are confirmed as:  $\mathbf{F}_b$  and  $\mathbf{M}_b$  for the roller,  $\mathbf{F}_{ir}$  and  $\mathbf{M}_{ir}$  for the inner ring and  $\mathbf{F}_{or}$  for the outer ring [5,26].

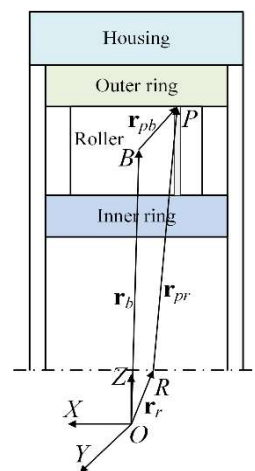


**Figure 1.** Interaction between a roller and outer ring.

## 2.2. Interaction between Outer Ring and Housing

The interaction between the outer ring and housing is expressed in Figure 2. The position and movement speed vectors for the outer ring are  $(y_{or}, z_{or})$  and  $(v_{ry}, v_{rz})$  and the related parameters for the housing are  $(y_h, z_h)$  and  $(v_{hy}, v_{hz})$ . Then, the position and movement speed between the outer ring and housing are:

$$\begin{cases} y_{rh} = y_{or} - y_h \\ z_{rh} = z_{or} - z_h \end{cases} \quad (6)$$

$$\begin{cases} v_{rhy} = v_{ry} - v_{hy} \\ v_{rhz} = v_{rz} - v_{hz} \end{cases} \quad (7)$$

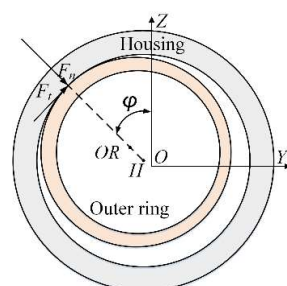


**Figure 2.** Interaction between outer ring and housing.

Then, the distance from the outer ring center to housing center is:

$$r_{rh} = \sqrt{y_{rh}^2 + z_{rh}^2} \quad (8)$$

The minimum distance can be described as:

$$\begin{cases} \sin \varphi = -\frac{y_{rh}}{r_{rh}} \\ \cos \varphi = \frac{z_{rh}}{r_{rh}} \end{cases} \quad (9)$$

The contact force between the outer ring and housing is given as:

$$\begin{cases} F_n = k_p(r_{rh} - e_p) - c_p(v_{rhx} \cos \varphi - v_{rhy} \sin \varphi) & r_{rh} > e_p \\ F_n = 0 & \text{other} \end{cases} \quad (10)$$

where,  $k_p$  is the contact stiffness between the outer ring and housing and  $c_p$  is the viscous damping relative to the tightening moment [22]. Later, the friction force between the outer ring and housing is:

$$F_t = \text{sign}(\mu_{rh} v_{rhx} \sin \varphi + v_{rhy} \cos \varphi) F_n \quad (11)$$

where,  $\mu_{rh}$  is friction coefficient. The forces on the outer ring in the  $x$ -direction and  $y$ -direction are:

$$\begin{cases} F_{ry} = F_n \sin \varphi + F_t \cos \varphi \\ F_{rz} = F_t \sin \varphi - F_n \cos \varphi \end{cases} \quad (12)$$

Additionally, the forces acting on housing in the  $x$ -direction and  $y$ -direction are:

$$\begin{cases} F_{hy} = -F_{ry} \\ F_{hz} = -F_{rz} \end{cases} \quad (13)$$

### 2.3. The Model for Localized Defects in the Bearing

In the presence of localized defects on the surface of the bearing components, the overlap between a roller and ring is affected, which can be described as:

$$\delta = \delta - \delta_d \quad (14)$$

where,  $\delta_d$  is the overlap caused by localized defects. When there is a localized defect on the ring surface, the relative overlap is:

$$\delta_d = \begin{cases} H_e \sin\left(\frac{\pi}{\varphi_d}(\text{mod}(\varphi_i, 2\pi) - \varphi_0)\right) & 0 \leq (\text{mod}(\varphi_i, 2\pi) - \varphi_0) \leq \varphi_d \\ 0 & \text{other} \end{cases} \quad (15)$$

where,  $H_e$  is maximal additional deformation,  $\varphi_d$  is the arc length for the defect area and  $\varphi_0$  is the initial position. When there is a localized defect on the roller surface, the defect overlap can be expressed as:

$$\delta_d = \begin{cases} H_e \sin(\pi(\text{mod}(\varphi_i, 2\pi) - \varphi_0)/\varphi_d) & 0 \leq \text{mod}(\varphi_b - \varphi_0) \leq \varphi_d \text{ for outer ring} \\ H_d & 0 \leq (\text{mod}(\varphi_b, 2\pi) - \pi - \varphi_0) \leq \varphi_d \text{ for inner ring} \\ 0 & \text{other} \end{cases} \quad (16)$$

where,  $H_d$  is the defect depth. More details are provided in Ref. [5].



## 2.4. Bearing System Equations

When the force and moment of bearing parts are found, the bearing system equations can be described based on the Newton–Euler theory [26]. In the inertial frame, the translational equations for the inner ring and rotor are:

$$\begin{cases} m_r \ddot{y}_{ir} = F_{ir2} + m_e e \omega_r^2 \sin \omega_r t \\ m_r \ddot{z}_{ir} = F_{ir3} - m_r g - F_r + m_e e \omega_r^2 \cos \omega_r t \end{cases} \quad (17)$$

where,  $m_r$  is the mass of the inner ring and rotor,  $F_r$  represents the external radial loads,  $F_{ir2}$  and  $F_{ir3}$  are the second and third parts of the force vector  $\mathbf{F}_{ir}$ ,  $g$  is the gravitational acceleration,  $m_e$  is the unbalanced mass,  $e$  is the unbalanced distance from the rotor center,  $\omega_r$  is the rotor rotation speed of rotor and  $t$  is the time. Then, the translational equations for the  $i$ th roller in the inertial cylindrical frame are given by:

$$\begin{cases} m_b \ddot{r}_b - m_b r_b \dot{\theta}_b^2 = F_{b3} - m_b g \sin \theta_b \\ m_b r_b \ddot{\theta}_b + 2m_b \dot{r}_b \dot{\theta}_b = -F_{b2} - m_b g \cos \theta_b \end{cases} \quad (18)$$

where,  $m_b$  is the roller mass,  $r_b$  is the radial displacement,  $\theta_b$  is the circumferential angle and  $F_{b2}$  and  $F_{b3}$  are the second and third parts of the force vector  $\mathbf{F}_b$ . Then, in the inner ring-fixed or roller-fixed frame, the rotate equations for inner ring or the roller can be written as:

$$I \dot{w}_1 = M_1 \quad (19)$$

where,  $I$  is the axial inertia moment for inner ring or the roller,  $w_1$  is the angular velocity,  $M_1$  is the first component of the torque vector  $\mathbf{M}_{ir}$  or  $\mathbf{M}_b$ . The translational equations for the outer ring in the inertial frame are:

$$\begin{cases} m_{or} \ddot{y}_{or} = F_{or2} + F_{ry} \\ m_{or} \ddot{z}_{or} = F_{or3} + F_{rz} - m_{or} g \end{cases} \quad (20)$$

where,  $m_{or}$  is the outer ring mass.

Additionally, as seen in Figure 3, the translational equations for housing are expressed as:

$$\begin{cases} m_h \ddot{y}_h + k_{hy} y_h + c_{hy} \dot{y}_h = F_{hy} \\ m_h \ddot{z}_h + k_{hz} z_h + c_{hz} \dot{z}_h = F_{hz} - m_h g \end{cases} \quad (21)$$

where,  $m_h$  is the housing mass,  $k_{hy}$  and  $k_{hz}$  represent the housing stiffness,  $c_{hy}$  and  $c_{hz}$  are the damping coefficients.

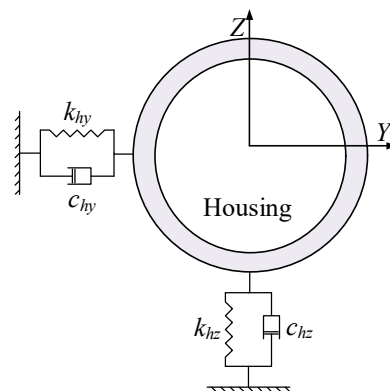


Figure 3. The housing model.

## 3. Results

After obtaining the proposed model, a flow chart of the whole process was configured and is provided in Figure 4. The displacements and velocities of the bearing parts were

acquired by the quasi-static model for initial values and Equations (1)–(13) were used for calculating the interactions between bearing components [26]. Additionally, during the process of calculation, defect models (Equations (14)–(16)) were considered. Then, the forces and moments acting on the bearing components were obtained, and were substituted into the bearing system Equations (17)–(21). Using FORTRAN programming, the fourth-order Runge–Kutta integration method with variable steps was used for solving the system equations, and the initial time step was set as  $1.0 \times 10^{-5}$  s. Lastly, displacements, velocities and accelerations of the bearing parts at different times were acquired, and the effect of fit clearance on the bearing vibration characteristics was discussed.

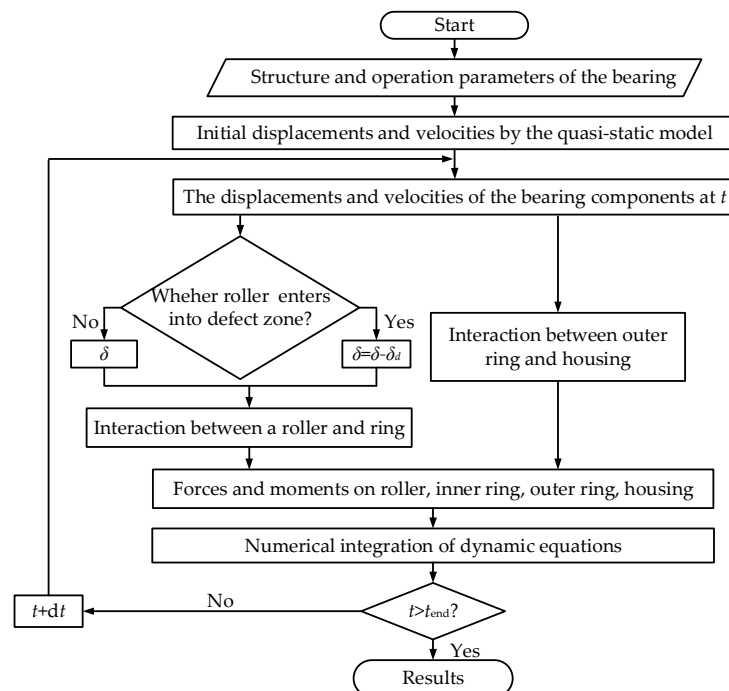


Figure 4. The flow chart for the whole process.

To verify the current model, the experiment was carried out and compared with the simulation results. Figure 5 shows the test rig, for which a motor, torque transducer, coupler, supporting bearing 1, counterweight pan, supporting bearing 2, force sensor, loading device, acceleration sensor, tested bearing and feeler gauge were included. The motor was used for the input speed of the tested bearing, and fit clearance was measured using the feeler gauge. NSK NUP205ECP was selected as the tested bearing and localized defects were divided into the inner ring defect and outer ring defect, which can be seen in Figure 6. The defects were manufactured using wire-electrode cutting. The defect width is 0.2 mm, the defect depth is 0.5 mm, and the defect length is the same as the bearing width.

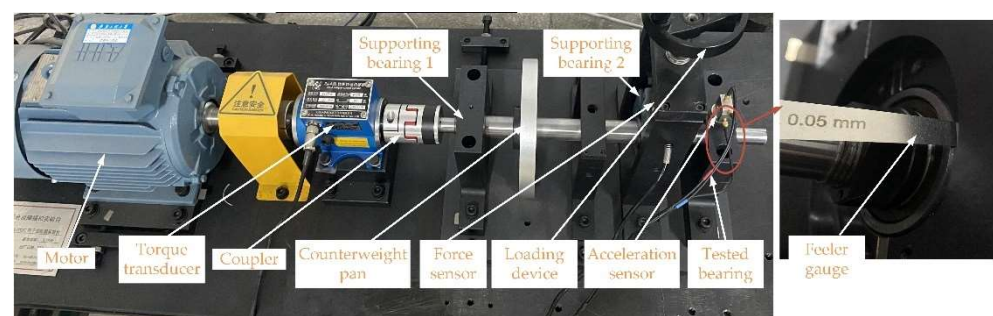
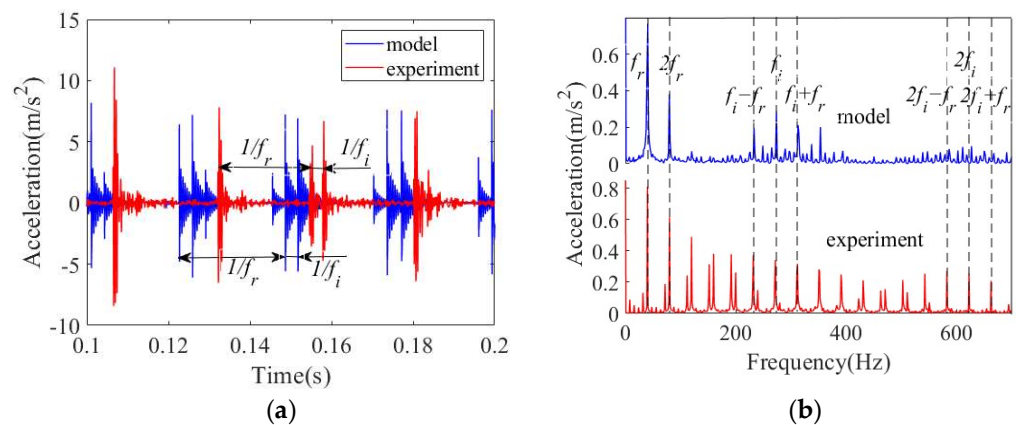


Figure 5. The test rig for the defective bearing with fit clearance.



**Figure 6.** Defective bearings: (a) localized defects on inner ring; (b) localized defects on outer ring.

The load and input speed for the test bearing were set as 800 N and 2400 rpm, with fit clearance as 0.05 mm. In the compared model, the housing stiffness and damping coefficient were set as  $1.5 \times 10^7$  N/m and 1800 Ns/m [18], the contact stiffness and friction coefficient between outer ring and housing were  $1.5 \times 10^7$  N/m and 0.3 and the viscous damping was 1800 Ns/m. For the bearing components, the density was  $7.75 \times 10^3$  kg/m<sup>3</sup>, the elasticity modulus was  $2.0 \times 10^7$  N/m<sup>2</sup> and the Poisson ratio was 0.25. In the experiment, the vertical acceleration was obtained using the acceleration sensor, and the sampling frequency was 30 kHz. Compared with the spectrum signal, defect frequencies in the envelope spectrum were more obvious. Next, the time domain signals were processed by the envelope spectrum for frequency components in the bearing. On the basis of the equations in Appendix A, the shaft frequency  $f_r$  was 40 Hz, cage frequency  $f_c$  was 16.1 Hz, roller passing outer raceway frequency  $f_o$  was 209.4 Hz and the roller passing inner raceway frequency  $f_i$  was 310.6 Hz. The comparison results for the inner ring defect can be seen in Figure 7, where there are periodic shock zones in the acceleration signals of the model and experiment, the time interval between shock zones is the same as  $1/f_r$ , and the time lag between the impacts in the shock zone is in line with  $1/f_i$ ; and the rotor frequency  $f_r$ , inner ring defect frequency  $f_i$  and the harmonic frequencies  $2f_r, f_i - f_r, f_i + f_r, 2f_i - f_r, 2f_i, 2f_i + f_r$  can be found in the envelope spectrums.



**Figure 7.** The comparison results for time-domain and frequency responses under inner ring defect: (a) acceleration signals; (b) envelope spectrum.

Figure 8 shows the comparison results for the outer ring defect. In this figure, periodic impacts are found in the acceleration signals of the model and experiment, the time interval is in accordance with  $1/f_o$ ; and cage frequency  $f_c$ , rotor frequency  $f_r$ , outer ring defect frequency  $f_o$  and the harmonic frequencies  $2f_c, f_o - f_c, f_o + f_c, 2f_o - f_c, 2f_o, 2f_o + f_c$  are present in the envelope spectrums. The frequency values are nearly in agreement and there is only a slight difference in the amplitudes. The difference was caused by the uncertain actual parameters, which were only neglected in the calculated model. Meanwhile, in the experiment, contact interfaces were present in the bearing, which affected the bearing

vibration characteristic. Compared with the model, the amplitude for sidebands at the cage frequency of outer defect frequency was very little. Thus, the constructed model is validated through the abovementioned comparison results.

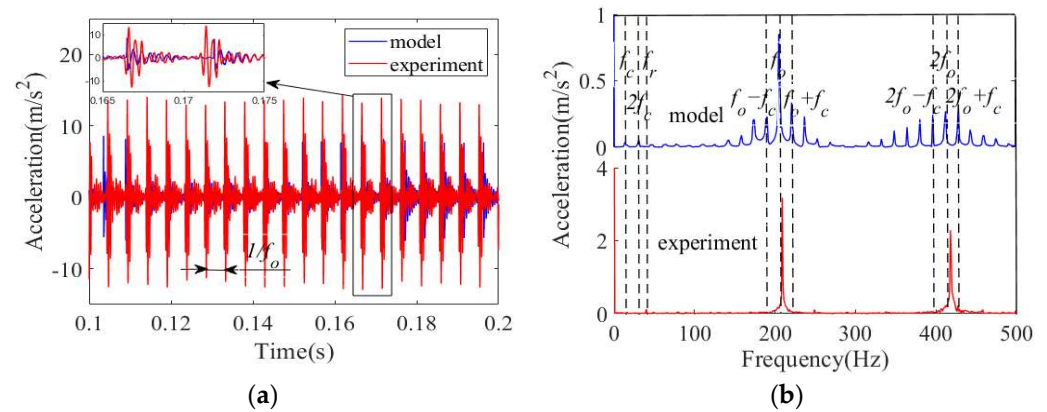


**Figure 8.** The comparison results for time-domain and frequency responses under outer ring defect: (a) acceleration signals; (b) envelope spectrum.

#### 4. Discussion

Following the verification of the calculated model, the effects of fit clearance on the vibration characteristic of the bearing with the inner ring defect, outer ring defect and roller defect are discussed in this section. In the defects, the width was 0.2 mm, the depth was 0.1 mm, the length was 2 mm, with the initial position being  $\pi$ . The above material parameters are also analyzed in this section, and other structure parameters for the simulated bearing are listed in Table 1, while the working conditions and defect frequencies are provided in Tables 2 and 3, respectively. In addition, the other parameters related to fit clearance mainly contain housing stiffness, the friction coefficient between the outer ring and housing and viscous damping. Housing stiffness is in direct correlation to the bearing acceleration, which was used for the bearing vibration analysis [24]. Thus, housing stiffness represents the first analysis parameter, followed by fit clearance, the friction coefficient and viscous damping in the sequence.

**Table 1.** Structure parameters for the simulated bearing.

Parameters	Value
Pitch diameter $d_m$ /mm	60
Bearing width $L_r$ /mm	18
Roller number $N_b$	14
Roller length $L_b$ /mm	10
Roller diameter $d_b$ /mm	10
Central flat land $L_p$ /mm	5
Roller corner radius $r_c$ /mm	0.4
Crown radius $R_r$ /mm	1500
Radial clearance $C_r$ /mm	0
The unbalanced mass $m_e$ /kg	0.02
The unbalanced distance from the rotor center $e$ /mm	5
Roller mass $m_b$ /kg	0.006
Mass of inner ring and rotor $m_r$ /kg	0.164
Mass of outer ring $m_{or}$ /kg	1
Mass of housing $m_h$ /kg	8
Axial inertia moment of roller $I_b$ /kgm <sup>2</sup>	$7.6 \times 10^{-8}$
Contact stiffness between outer ring and housing $k_p$ /N/m	$1.5 \times 10^7$

**Table 2.** Working conditions for the simulated bearing.

Parameters	Value
Load $F_r$ /N	500
Input speed $w_r$ /r/min	4000

**Table 3.** Defect frequencies for the simulated bearing.

Frequency	Value
Rotor frequency $f_c$ /Hz	66.67
Cage frequency $f_r$ /Hz	27.78
Outer defect frequency $f_o$ /Hz	388.89
Inner defect frequency $f_i$ /Hz	544.44
Roller defect frequency $f_b$ /Hz	194.44
Cage passing inner ring frequency $f_{ir}$ /Hz	38.89

#### 4.1. Vibration Characteristics of a Cylindrical Roller Bearing with Fit Clearance and Inner Ring Defect

##### 4.1.1. Effect of Housing Stiffness

The following parameters were used to investigate effect of housing stiffness on the bearing vibration response: fit clearance of 50  $\mu\text{m}$ , housing damping of 1800 Ns/m, and a friction coefficient between the outer ring and housing of 0.3, viscous damping of 1800 Ns/m and a phase difference between the defect location and unbalanced force of  $0^\circ$ . The housing stiffness is strongly associated with materials. Thereupon, the housing stiffness was set as  $2.24 \times 10^6$  N/m,  $1.5 \times 10^7$  N/m and  $2.0 \times 10^8$  N/m [18,22,24], which correspond to case1, case2 and case3 for the convenient analysis.

The time-domain and frequency responses of the bearing housing are shown in Figure 9. When the housing stiffness was  $2.24 \times 10^6$  N/m, a sinusoidal fluctuation occurred in terms of the acceleration responses, but the fluctuation amplitude decreased with the housing stiffness from  $1.5 \times 10^7$  N/m to  $2.0 \times 10^8$  N/m. The time interval between two fluctuation peaks was  $1/f_r$ . In the fluctuated acceleration signals, periodic shock zones were found, and the time lag between them was also  $1/f_r$ . Meanwhile, the time interval between the impacts in the shock zone was  $1/f_i$ . The RMS (Root Mean Square) was used to describe the acceleration signal, and decreased with the housing stiffness from  $2.24 \times 10^6$  N/m to  $2.0 \times 10^8$  N/m. Then, in the envelope spectrums,  $f_r$ ,  $f_i - f_r$ ,  $f_i$ ,  $f_i + f_r$ ,  $2f_i - f_r$ ,  $2f_i$  and  $2f_i + f_r$  were found. The frequency amplitudes increased with increasing housing stiffness, and the amplitude of  $f_r$  was the largest. In order to illustrate the phenomenon, the local acceleration signal and forces in the bearing are provided in Figure 10. In terms of the time of the shock, the housing stiffness  $2.0 \times 10^8$  N/m was earliest, followed by  $1.5 \times 10^7$  and  $2.24 \times 10^6$  relative to the impact force. When the radial load acts on the cylindrical roller bearing, contact zones between the roller and rings are classified as either a loaded zone or unloaded zone [5]. The roller can contact with the inner ring and outer ring simultaneously in the loaded zone. If the roller interacts with the defective inner ring, impact force is generated. Then, the impact force is delivered to the outer ring. Meanwhile, the sinusoidal fluctuation can also be found in the contact force, while the impact force only exists in the fluctuation valley, which is the loaded zone.



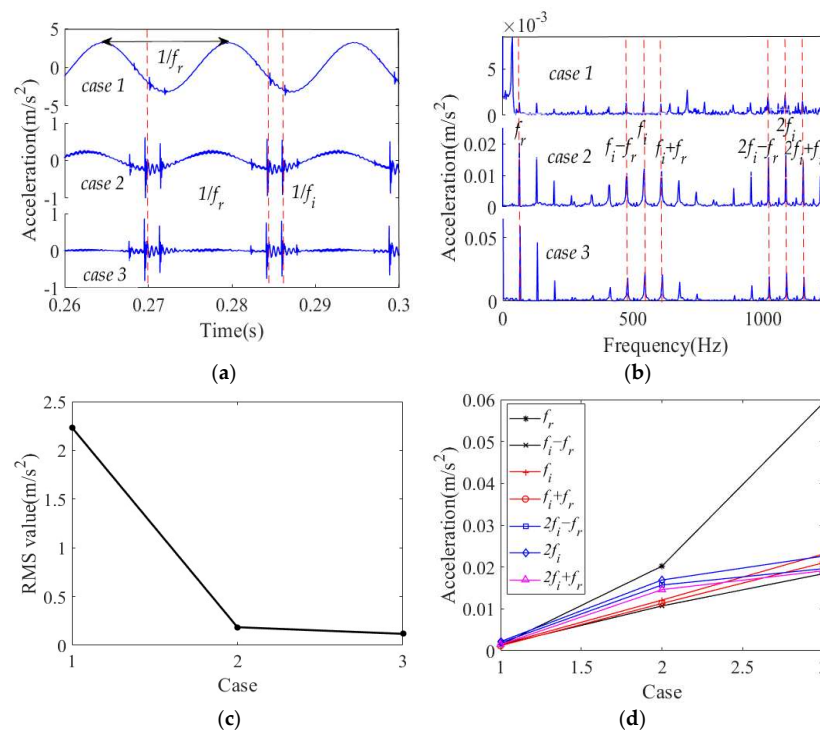


**Figure 9.** The time-domain and frequency responses of the bearing housing under inner ring defect and different housing stiffness: (a) acceleration signals; (b) envelope spectrum; (c) RMS; (d) amplitudes of  $f_r$ ,  $f_i - f_r$ ,  $f_i$ ,  $f_i + f_r$ ,  $2f_i - f_r$ ,  $2f_i$ ,  $2f_i + f_r$ .

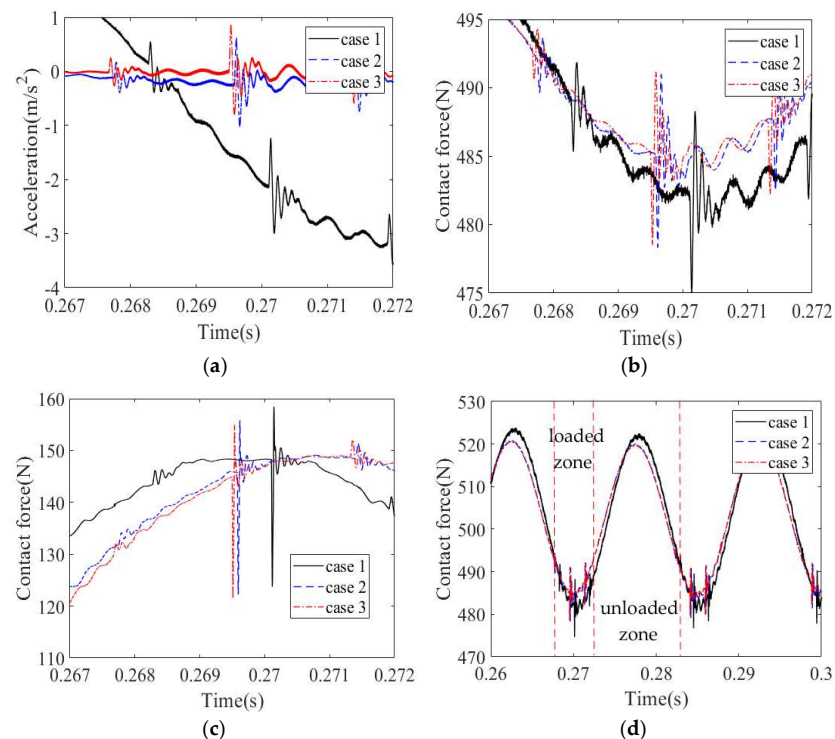


**Figure 10.** The acceleration signal and forces in the bearing under inner ring defect and housing stiffness: (a) housing acceleration signal from 0.267 s to 0.272 s; (b) contact force between outer ring and housing from 0.267 s to 0.272 s; (c) contact force between the roller and outer ring from 0.267 s to 0.272 s; (d) contact force between outer ring and housing from 0.26 s to 0.3 s.

#### 4.1.2. Effect of Fit Clearance

In this section, we analyze fit clearances of 0  $\mu\text{m}$ , 50  $\mu\text{m}$ , 100  $\mu\text{m}$ , 150  $\mu\text{m}$  and 200  $\mu\text{m}$  and housing stiffness of  $1.5 \times 10^7$  N/m, while other parameters are same as that in the above housing stiffness analysis. The effect of fit clearance on the bearing vibration characteristics was studied, for which the results are listed in Figure 11. The RMS values increase with fit clearance from 0  $\mu\text{m}$  to 200  $\mu\text{m}$ , and the amplitude of  $f_r$  also increased. Amplitudes of  $2f_i - f_r$ ,  $2f_i$  and  $2f_i + f_r$  increased with fit clearance from 0  $\mu\text{m}$  to 100  $\mu\text{m}$ , and then decreased. There are opposite laws for the amplitudes of  $f_i - f_r$ ,  $f_i$  and  $f_i + f_r$ , and the largest amplitude was found for  $f_r$ . The shock time for a fit clearance of 0  $\mu\text{m}$  was earliest, followed by 50  $\mu\text{m}$ , 100  $\mu\text{m}$ , 150  $\mu\text{m}$  and 200  $\mu\text{m}$ . Meanwhile, the same trend was detected in the contact force between the outer ring and housing.

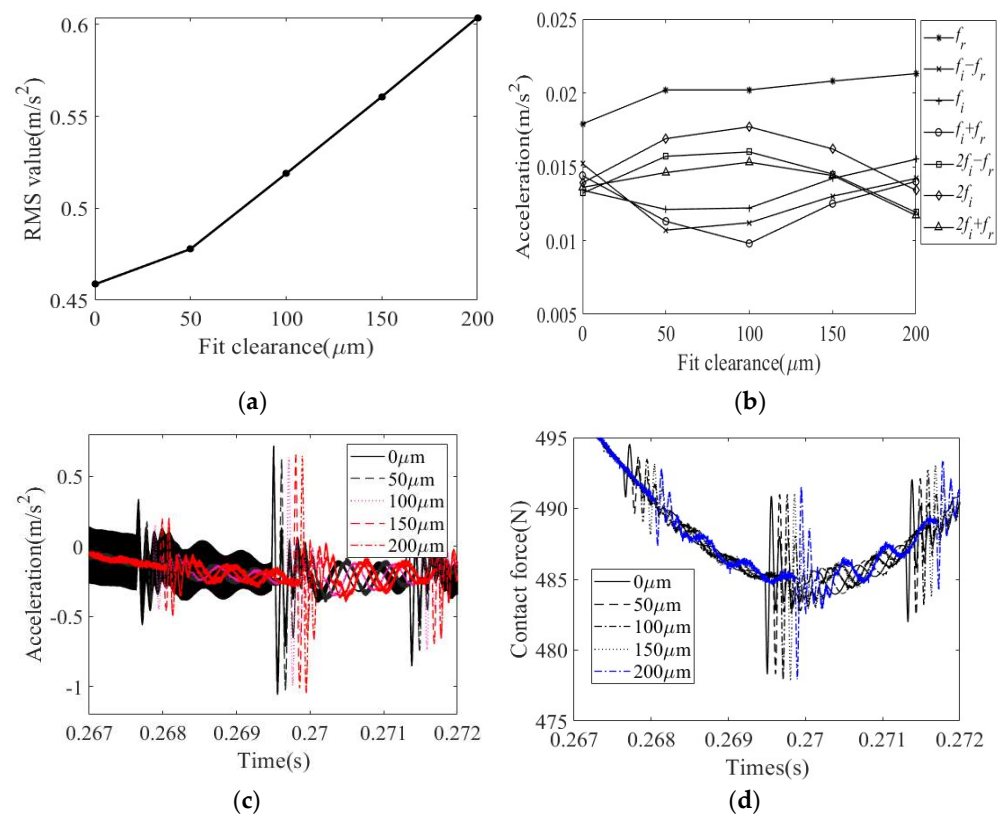


**Figure 11.** The vibration characteristics of the bearing under inner ring defect and fit clearance: (a) RMS; (b) amplitudes of  $f_r$ ,  $f_i - f_r$ ,  $f_i$ ,  $f_i + f_r$ ,  $2f_i - f_r$ ,  $2f_i$ ,  $2f_i + f_r$ ; (c) housing acceleration signal from 0.267 s to 0.272 s; (d) contact force between outer ring and housing from 0.267 s to 0.272 s.

#### 4.1.3. Effect of Friction Coefficient

The housing stiffness was set as  $1.5 \times 10^7$  N/m, while the friction coefficient between outer ring and housing was set as 0.1, 0.2, 0.3, 0.4 and 0.6. The other parameters are the same as in the above housing stiffness analysis. The vibration characteristics of the bearing under the inner ring defect and friction coefficient are given in Figure 12. RMS values increased with the friction coefficient from 0.1 to 0.6. There were smaller differences in the change rules of frequency amplitudes. Amplitudes of  $f_r$ ,  $f_i$  and  $2f_i$  increased with the friction coefficient from 0.1 to 0.6, and amplitudes of other frequencies decreased. Meanwhile, among all frequency amplitudes, the largest was for  $f_r$ . Small differences can also be found in the acceleration signal and contact force between the outer ring and housing. However, as the shock peak increases, the fluctuation amplitudes increase with the friction coefficient from 0.1 to 0.6.



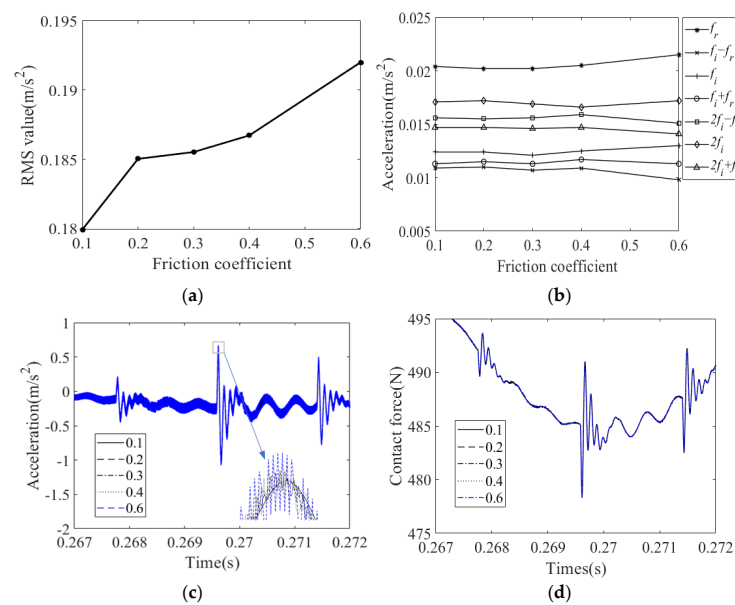


**Figure 12.** The vibration characteristics of the bearing under inner ring defect and friction coefficient: (a) RMS; (b) amplitudes of  $f_r$ ,  $f_i - f_r$ ,  $f_i$ ,  $f_i + f_r$ ,  $2f_i - f_r$ ,  $2f_i$ ,  $2f_i + f_r$ ; (c) housing acceleration signal from 0.267 s to 0.272 s; (d) contact force between outer ring and housing from 0.267 s to 0.272 s.

#### 4.1.4. Effect of Viscous Damping

The housing stiffness was set as  $1.5 \times 10^7$  N/m, while viscous damping was set as 0 Ns/m, 200 Ns/m, 1800 Ns/m, 3400 Ns/m and 5000 Ns/m. The other parameters were the same as in the above housing stiffness analysis. Figure 13 shows the vibration characteristics of the bearing under the inner ring defect and viscous damping. When viscous damping was set from 0 Ns/m to 5000 Ns/m, the RMS and frequency amplitudes increased. The fluctuated amplitudes for viscous damping 0 Ns/m were largest, and other amplitudes reduced from 3400 Ns/m to 5000 Ns/m in turn. The same laws were also seen in the contact force between the outer ring and housing.

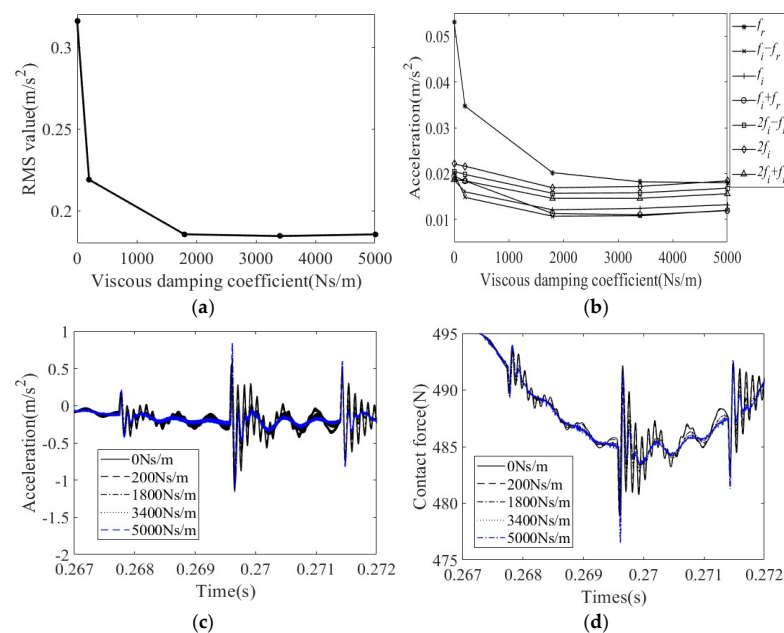


**Figure 13.** The vibration characteristics of the bearing under inner ring defect and viscous damping: (a) RMS; (b) amplitudes of  $f_r$ ,  $f_i - f_r$ ,  $f_i$ ,  $f_i + f_r$ ,  $2f_i - f_r$ ,  $2f_i$ ,  $2f_i + f_r$ ; (c) housing acceleration signal from 0.267 s to 0.272 s; (d) contact force between outer ring and housing from 0.267 s to 0.272 s.

#### 4.1.5. Effect of Phase Difference

Due to the inner ring defect, a phase difference between the defect location and rotor unbalanced force exists, which affects the force acting on the bearing immediately. Thus, the initial phase of the unbalanced force changes with the following phase differences:  $0^\circ$ ,  $45^\circ$ ,  $90^\circ$ ,  $135^\circ$  and  $180^\circ$ . The effect of the phase difference on the vibration characteristics of the bearing was investigated, which can be seen in Figure 14. When the phase difference is set between  $0^\circ$  and  $180^\circ$ , the generated force decreases constantly. Thus, the RMS, acceleration fluctuation amplitude and amplitude of  $f_r$  reduce. The amplitudes of other frequencies increase with the phase difference from  $0^\circ$  to  $90^\circ$ , then decrease. However, the amplitude of  $f_r$  was found to be largest. In the contact force between the outer ring and housing, the fluctuated phase changed with the phase difference, while the phases of  $0^\circ$  and  $180^\circ$  are in contrast.

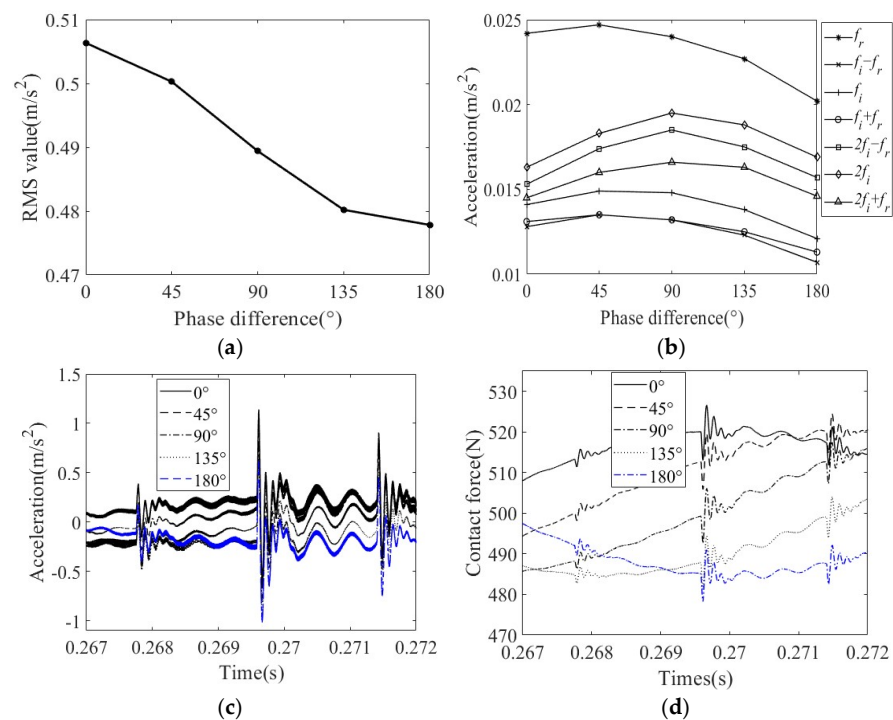


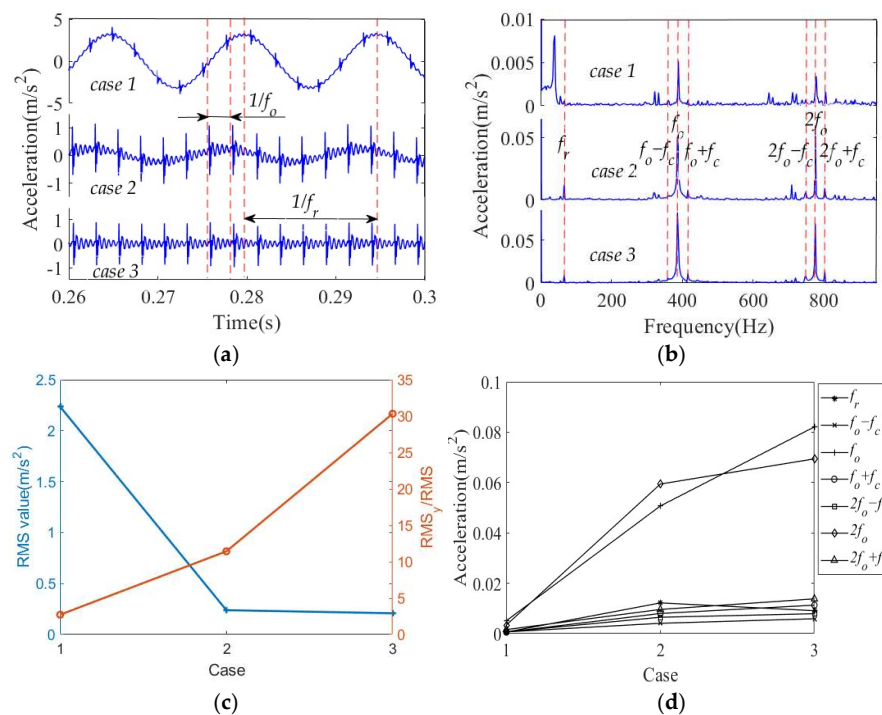
**Figure 14.** The vibration characteristics of the bearing under inner ring defect and unbalanced force: (a) RMS; (b) amplitudes of  $f_r$ ,  $f_i - f_r$ ,  $f_i$ ,  $f_i + f_r$ ,  $2f_i - f_r$ ,  $2f_i$ ,  $2f_i + f_r$ ; (c) housing acceleration signal from 0.267 s to 0.272 s; (d) contact force between outer ring and housing from 0.267 s to 0.272 s.

#### 4.2. Vibration Characteristics of a Cylindrical Roller Bearing with Fit Clearance and Outer Ring Defect

In this section, the analysis conditions studies are same as for the inner ring defect.

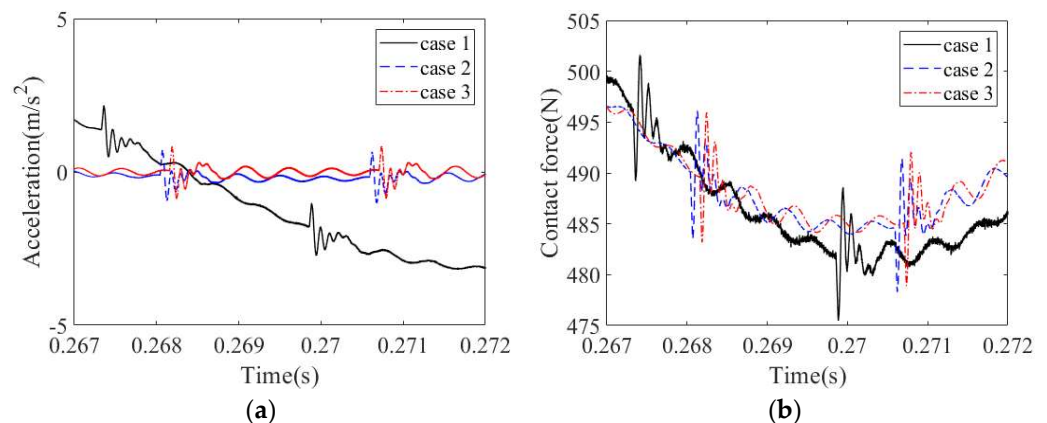
##### 4.2.1. Effect of Housing Stiffness

Figure 15 provides time-domain and frequency responses of the bearing housing under the outer ring defect and different housing stiffness. The sinusoidal fluctuation laws of the acceleration responses can also be found. Periodic impacts were detectable, and the time interval between the two impact peaks was  $1/f_o$ . RMS also decreased with increasing housing stiffness. In order to obtain the location of the outer ring defect,  $\text{RMS}_y/\text{RMS}$  is typically used as an evaluation index, and  $\text{RMS}_y$  is the root mean square of the acceleration in the Y direction (horizontal direction) [27]. In this Figure,  $\text{RMS}_y/\text{RMS}$  increased with increasing housing stiffness.  $f_r$ ,  $f_o - f_c$ ,  $f_o$ ,  $f_o + f_c$ ,  $2f_o - f_c$ ,  $2f_o$  and  $2f_o + f_c$  can be found in the envelope spectrums, of which the most remarkable amplitudes are  $f_o$  and  $2f_o$ . The other frequency amplitudes increased with enhanced housing stiffness.



**Figure 15.** The time-domain and frequency responses of the bearing housing under outer ring defect and different housing stiffness: (a) acceleration signals; (b) envelope spectrum; (c) RMS and RMS<sub>y</sub>/RMS; (d) amplitudes of  $f_r$ ,  $f_o - f_c$ ,  $f_o$ ,  $f_o + f_c$ ,  $2f_o - f_c$ ,  $2f_o$ ,  $2f_o + f_c$ .

In Figure 16, the time of acceleration shock for the housing stiffness  $2.0 \times 10^8$  N/m is the earliest, followed by  $1.5 \times 10^7$  N/m and  $2.24 \times 10^6$  N/m. The phenomenon was caused by contact forces. In the bearing, the roller can always come into contact with the outer ring by centrifugal force. Thus, every roller passes through the defect zone of the outer ring, and impact force is generated. Then, the impact force is transferred to the housing by the interaction between the outer ring and housing, and an acceleration shock occurs in the housing.



**Figure 16.** Cont.

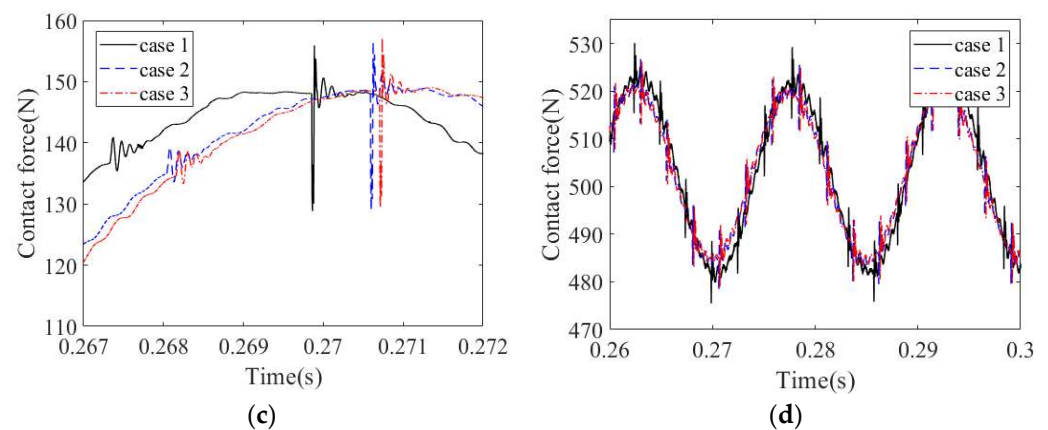


**Figure 16.** The acceleration signal and forces in the bearing under outer ring defect and housing stiffness: (a) housing acceleration signal from 0.267 s to 0.272 s; (b) contact force between outer ring and housing from 0.267 s to 0.272 s; (c) contact force between the roller and outer ring from 0.267 s to 0.272 s; (d) contact force between outer ring and housing from 0.26 s to 0.3 s.

#### 4.2.2. Effect of Fit Clearance

The effect of fit clearance on the bearing vibration characteristics with the defective outer ring is shown in Figure 17. RMS increases with fit clearance from 0  $\mu\text{m}$  to 200  $\mu\text{m}$ , but  $\text{RMS}_y/\text{RMS}$  decreases. The amplitudes of  $f_o$  and  $2f_o$  are much larger than of the other frequency amplitudes. The amplitude of  $f_o$  decreased with the fit clearance from 0  $\mu\text{m}$  to 100  $\mu\text{m}$ , and there an opposite trend occurred for the amplitude of  $2f_o$ . The amplitude of  $f_r$  increased with the fit clearance from 0  $\mu\text{m}$  to 50  $\mu\text{m}$  and from 150  $\mu\text{m}$  to 200  $\mu\text{m}$ , then decreased from 50  $\mu\text{m}$  to 150  $\mu\text{m}$ . The time of the impact for fit clearance 200  $\mu\text{m}$  is earliest, followed by 150  $\mu\text{m}$ , 100  $\mu\text{m}$ , 50  $\mu\text{m}$  and 0  $\mu\text{m}$ . The same trend occurred for the contact force between the outer ring and housing.

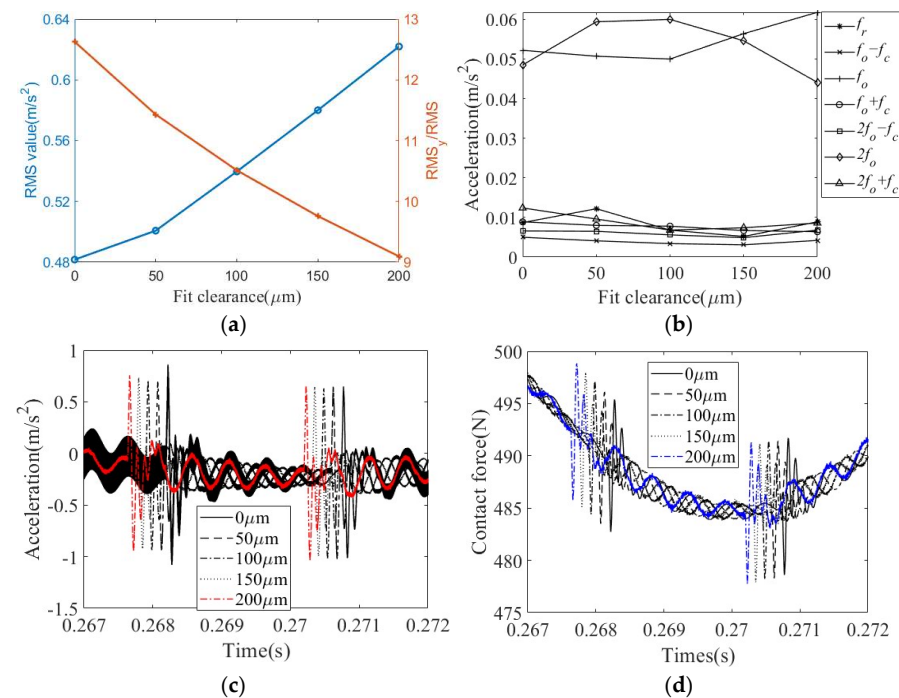


**Figure 17.** The vibration characteristics of the bearing under outer ring defect and fit clearance: (a) RMS and  $\text{RMS}_y/\text{RMS}$ ; (b) amplitudes of  $f_r$ ,  $f_o - f_c$ ,  $f_o$ ,  $f_o + f_c$ ,  $2f_o - f_c$ ,  $2f_o$ ,  $2f_o + f_c$ ; (c) housing acceleration signal from 0.267 s to 0.272 s; (d) contact force between outer ring and housing from 0.267 s to 0.272 s.

#### 4.2.3. Effect of Friction Coefficient

Vibration characteristics of the bearing under outer ring defect and the friction coefficient are shown in Figure 18. RMS and  $RMS_y/RMS$  increased with the friction coefficient from 0.1 to 0.6. Small differences in the change laws of the frequency amplitudes were also apparent. The amplitude of  $2f_o$  is the largest, followed by  $f_o$ ,  $f_r$ ,  $2f_o + f_c$ ,  $f_o + f_c$ ,  $2f_o - f_c$  and  $f_o - f_c$ . Meanwhile, clear rules could not be found in the acceleration signal and contact forces. However, the fluctuation amplitudes increased with the increased friction coefficient.

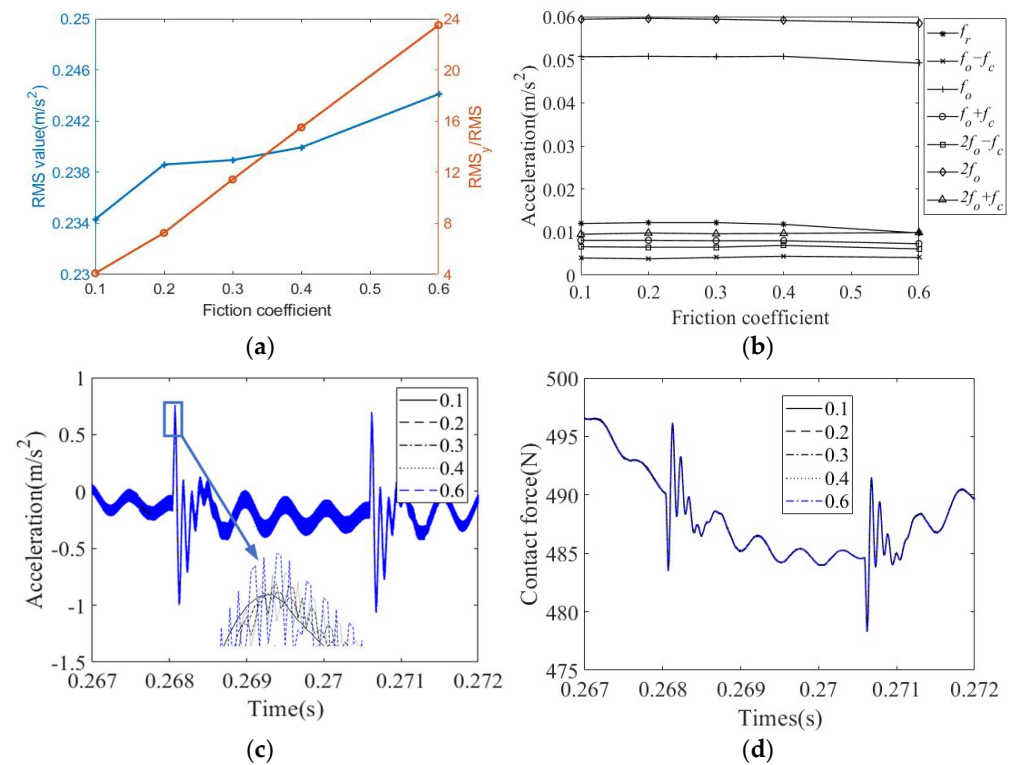


**Figure 18.** The vibration characteristics of the bearing under outer ring defect and friction coefficient: (a) RMS and  $RMS_y/RMS$ ; (b) amplitudes of  $f_r$ ,  $f_o - f_c$ ,  $f_o$ ,  $f_o + f_c$ ,  $2f_o - f_c$ ,  $2f_o$ ,  $2f_o + f_c$ ; (c) housing acceleration signal from 0.267 s to 0.272 s; (d) contact force between outer ring and housing from 0.267 s to 0.272 s.

#### 4.2.4. Effect of Viscous Damping

Figure 19 provides the vibration characteristics of the bearing under the outer ring defect and viscous damping. The RMS decreased with viscous damping from 0 Ns/m to 5000 Ns/m. The  $RMS_y/RMS$  increased with viscous damping from 0 Ns/m to 2000 Ns/m, but significant differences were not found from 2000 Ns/m to 5000 Ns/m. Amplitudes of  $2f_o$  and  $f_o$  increased from 0 Ns/m to 200 Ns/m, and then decreased. The amplitude of  $f_r$  decreased with the increasing viscous damping, and the change laws of other frequency amplitudes are not outstanding. The fluctuating amplitudes of housing accelerations decreased with increased viscous damping, while the same laws for contact force were also observable.



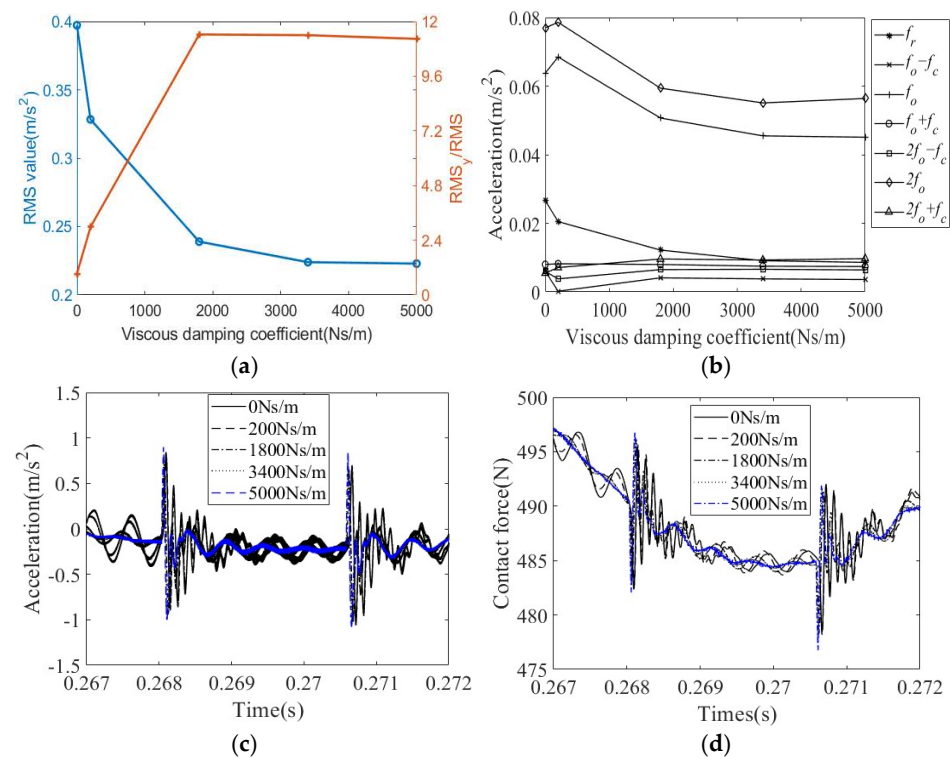


**Figure 19.** The vibration characteristics of the bearing under outer ring defect and viscous damping: (a) RMS and  $RMS_y/RMS$ ; (b) amplitudes of  $f_r$ ,  $f_o - f_c$ ,  $f_o$ ,  $f_o + f_c$ ,  $2f_o - f_c$ ,  $2f_o$ ,  $2f_o + f_c$ ; (c) housing acceleration signal from 0.267 s to 0.272 s; (d) contact force between outer ring and housing from 0.267 s to 0.272 s.

#### 4.2.5. Effect of Defect Location

In view of the loaded zone and unloaded zone in the cylindrical roller bearing, the effect of the outer ring defect location on the bearing vibration responses were investigated, with the defect location set as  $0^\circ$ ,  $45^\circ$ ,  $90^\circ$ ,  $135^\circ$  and  $180^\circ$ , for which the relative results are provided in Figure 20. The RMS increased with defect location from  $0^\circ$  to  $180^\circ$ , but contrary laws exist for  $RMS_y/RMS$ . The frequency amplitudes increased with the increasing defect location angle. For housing acceleration and contact force, the fluctuation amplitudes decreased with the increasing defect location angle. Meanwhile, except for  $135^\circ$  and  $180^\circ$ , the impacts for other defect location angle were not pronounced.

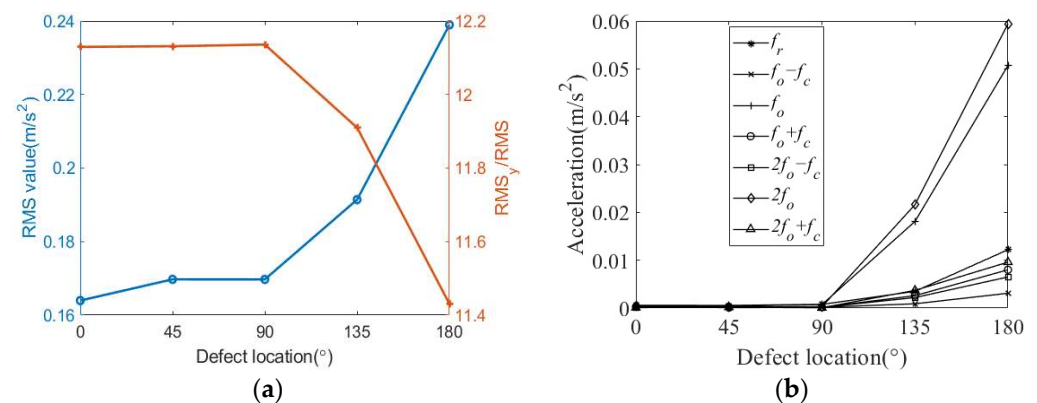


**Figure 20.** Cont.

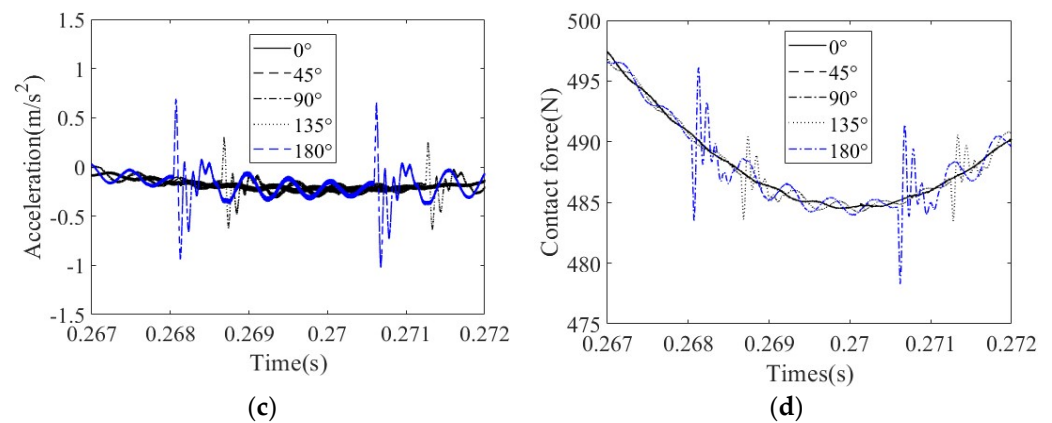


**Figure 20.** The vibration characteristics of the bearing under outer ring defect and defect location: (a) RMS and  $\text{RMS}_y/\text{RMS}$ ; (b) amplitudes of  $f_r, f_o - f_c, f_o, f_o + f_c, 2f_o - f_c, 2f_o, 2f_o + f_c$ ; (c) housing acceleration signal from 0.267 s to 0.272 s; (d) contact force between outer ring and housing from 0.267 s to 0.272 s.

#### 4.3. Vibration Characteristics of a Cylindrical Roller Bearing with Fit Clearance and Roller Defect

To analyze the vibration characteristics of the cylindrical roller bearing with the fit clearance and roller defect, the conditions for the inner ring defect were also used in this section, and the defect was set on the first roller.

##### 4.3.1. Effect of Housing Stiffness

The time-domain and frequency responses of the bearing housing under the roller defect and housing stiffness can be seen in Figure 21. The sinusoidal fluctuation laws for the acceleration responses were the same as those presented in Figure 9. The time interval between the two fluctuation peaks is  $1/f_r$ . In the acceleration signals, the time lag between the periodic shock zones was  $1/f_c$ , the time interval between the two adjacent impacts in the shock zone was  $1/2f_b$ , and the time lag of  $1/f_b$  was also found. RMS decreased with increased housing stiffness. In the envelope spectrums, there are  $f_c, f_b - f_c, f_b, f_b + f_c, 2f_b - f_c, 2f_b$  and  $2f_b + f_c$ , and amplitudes increased with the enhanced housing stiffness. The highest amplitude was  $f_c$ .

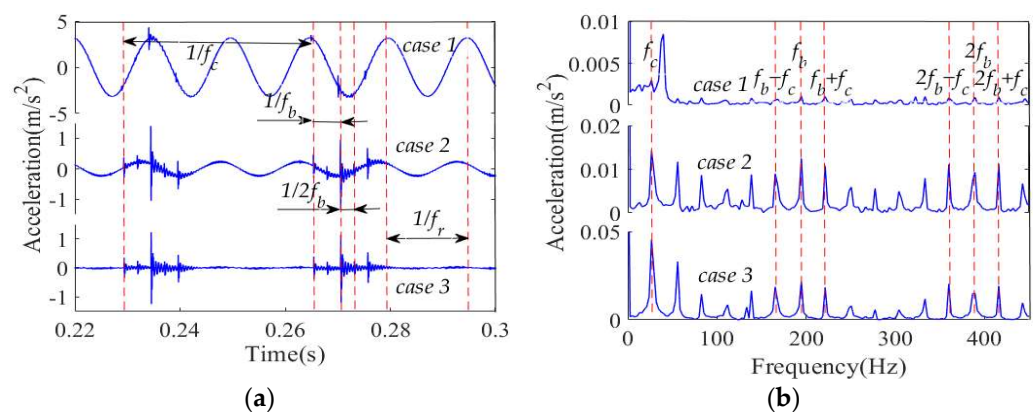


**Figure 21.** Cont.



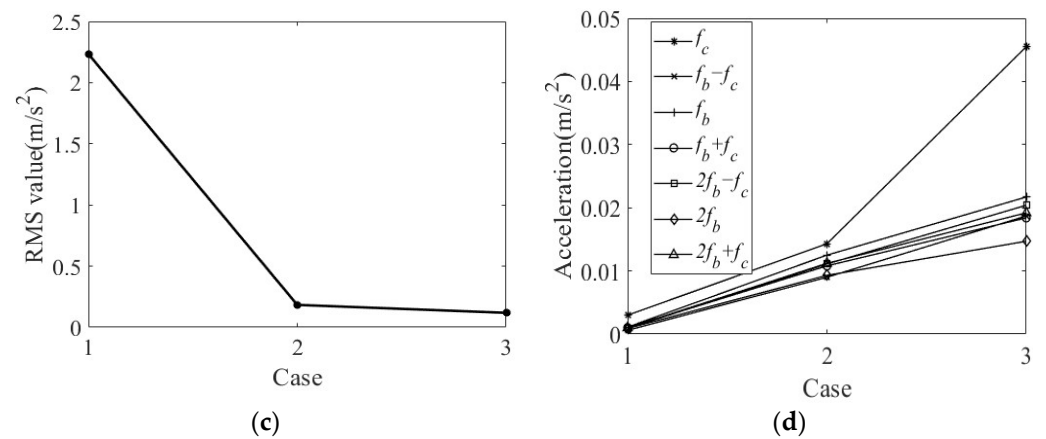


**Figure 21.** The time-domain and frequency responses of the bearing housing under roller defect and different housing stiffness: (a) acceleration signals; (b) envelope spectrum; (c) RMS; (d) amplitudes of  $f_c, f_b - f_c, f_b, f_b + f_c, 2f_b - f_c, 2f_b, 2f_b + f_c$ .

As listed in Figure 22, the shock time of housing stiffness  $2.24 \times 10^6$  N/m was earliest, followed by  $1.5 \times 10^7$  N/m and  $2.0 \times 10^8$  N/m. The above laws are relative to the contact forces. Compared with other defects, the defective roller rotated for  $2\pi$ , and came into contact with the outer ring and inner ring successively. Then, two shocks in a relatively short period of time occurred in the contact forces. Thus, there were also two shocks in the housing acceleration.

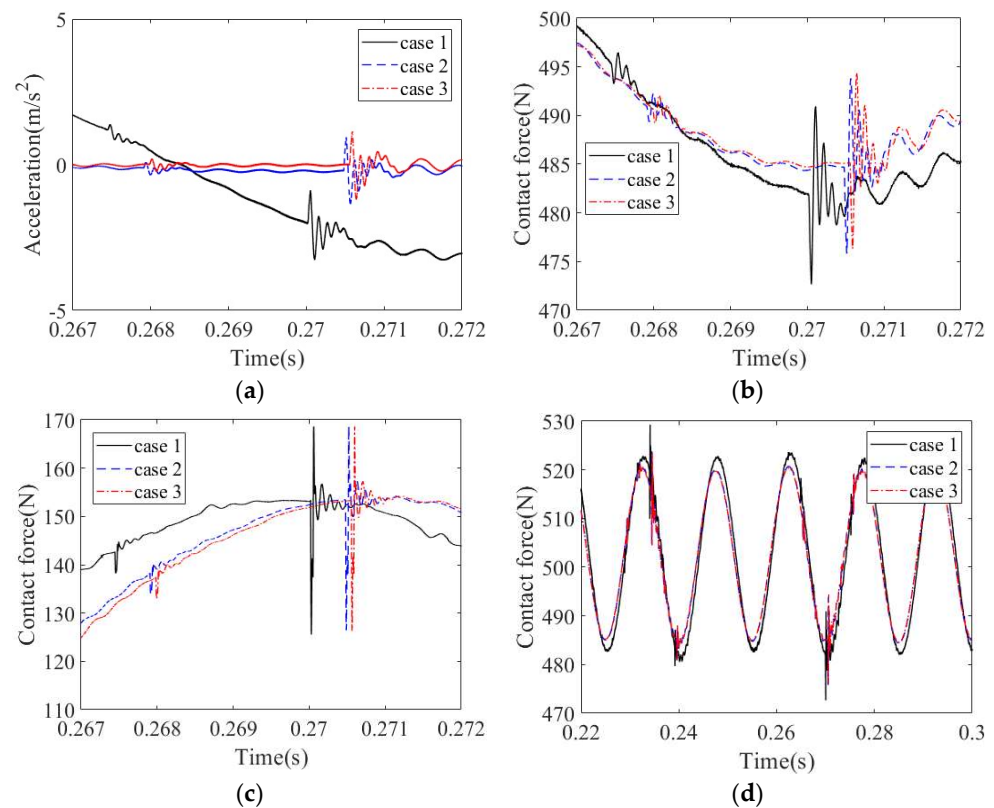


**Figure 22.** The acceleration signal and forces in the bearing under roller defect and housing stiffness: (a) housing acceleration signal from 0.267 s to 0.272 s; (b) contact force between outer ring and housing from 0.267 s to 0.272 s; (c) contact force between the roller and outer ring from 0.267 s to 0.272 s; (d) contact force between outer ring and housing from 0.22 s to 0.3 s.

#### 4.3.2. Effect of Fit Clearance

The bearing vibration characteristics with a defective outer ring and different fit clearances are listed in Figure 23. RMS increased with an increasing fit clearance. The amplitudes of  $f_c$ ,  $2f_b - f_c$  and  $f_b - f_c$  decreased, while the other frequency amplitudes increased. The amplitude of  $f_c$  was the largest. The time of the impact for a fit clearance of 200  $\mu\text{m}$  was the earliest, followed by 150  $\mu\text{m}$ , 100  $\mu\text{m}$ , 50  $\mu\text{m}$  and 0  $\mu\text{m}$ . The same trend for contact forces between the outer ring and housing exists.

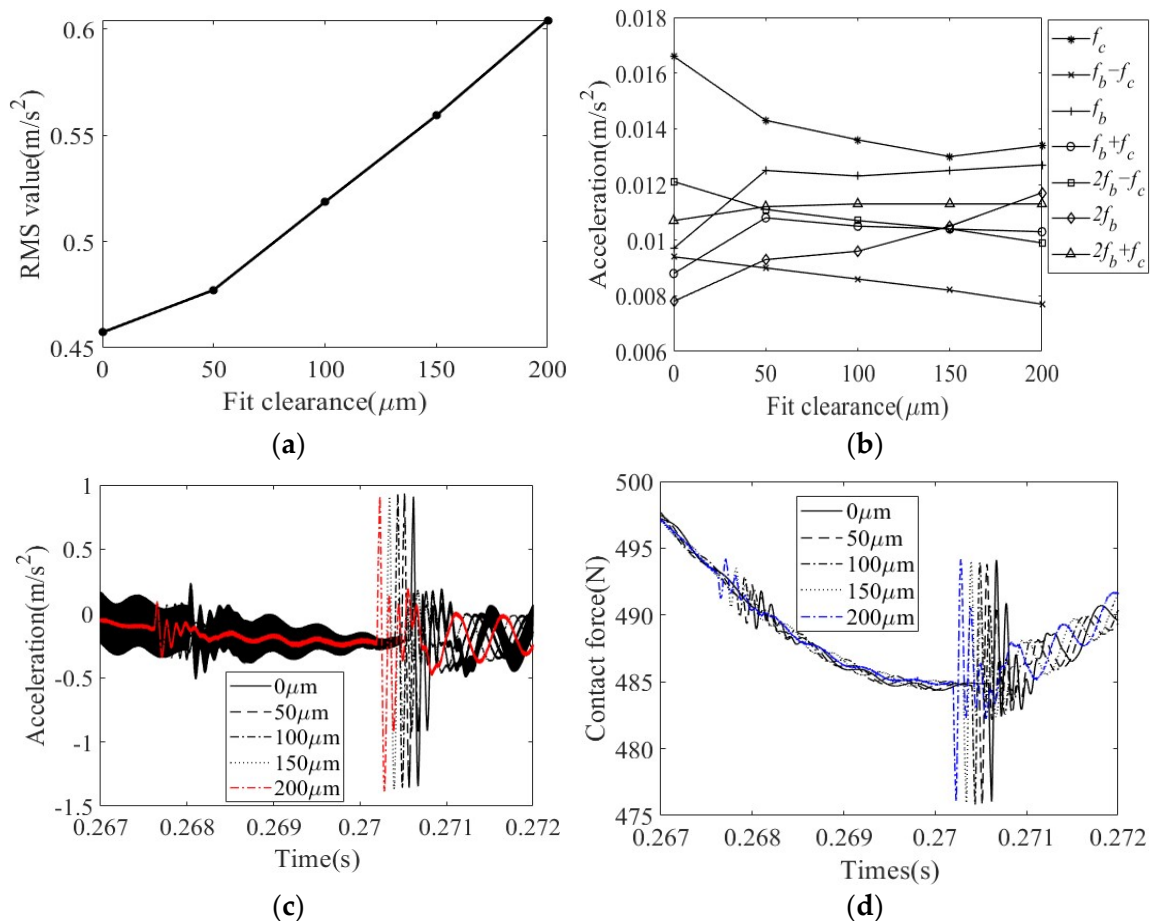


**Figure 23.** The vibration characteristics of the bearing under roller defect and fit clearance: (a) RMS; (b) amplitudes of  $f_c$ ,  $f_b - f_c$ ,  $f_b$ ,  $f_b + f_c$ ,  $2f_b - f_c$ ,  $2f_b$ ,  $2f_b + f_c$ ; (c) housing acceleration signal from 0.267 s to 0.272 s; (d) contact force between outer ring and housing from 0.267 s to 0.272 s.

#### 4.3.3. Effect of Friction Coefficient

The vibration characteristics of the bearing under the roller defect and friction coefficient are shown in Figure 24. The RMS values increased with the friction coefficient. The amplitude laws of  $f_c$ ,  $f_b - f_c$ ,  $f_b$ ,  $f_b + f_c$ ,  $2f_b - f_c$ ,  $2f_b$  and  $2f_b + f_c$  were not regular. Additionally, obvious rules could not be seen in the acceleration signal and contact force between the outer ring and housing. However, the fluctuation amplitudes also increased with the magnified friction coefficient.

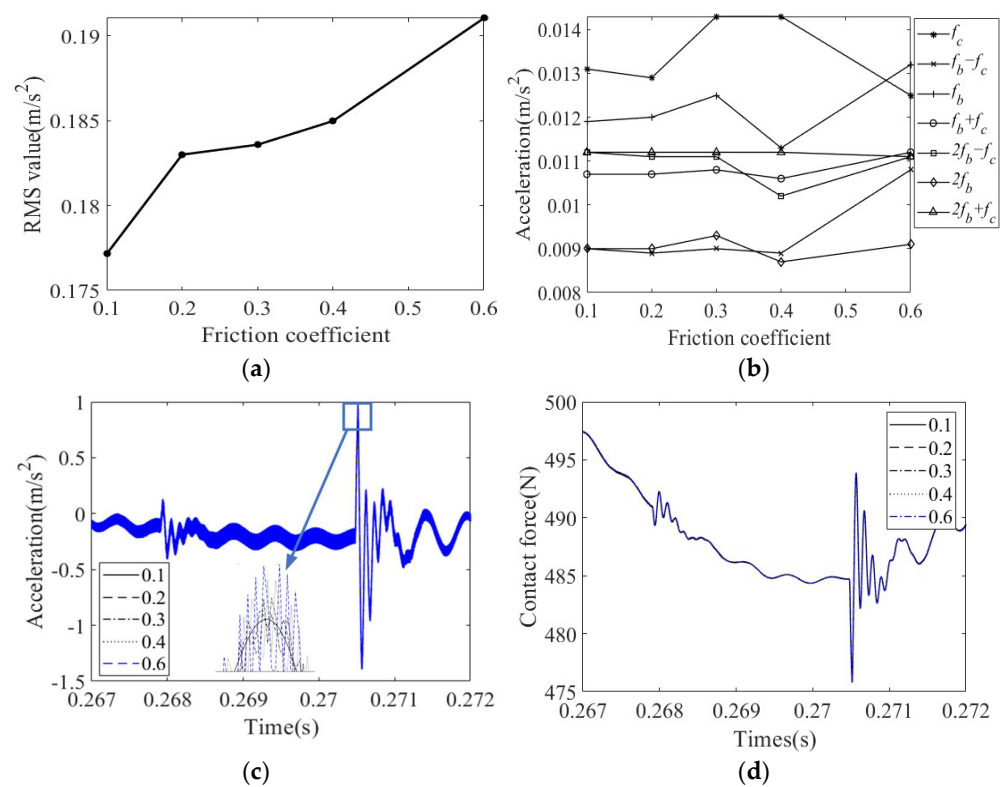


**Figure 24.** The vibration characteristics of the bearing under roller defect and friction coefficient: (a) RMS; (b) amplitudes of  $f_c$ ,  $f_b - f_c$ ,  $f_b$ ,  $f_b + f_c$ ,  $2f_b - f_c$ ,  $2f_b$ ,  $2f_b + f_c$ ; (c) housing acceleration signal from 0.267 s to 0.272 s; (d) contact force between outer ring and housing from 0.267 s to 0.272 s.

#### 4.3.4. Effect of Viscous Damping

Figure 25 shows the vibration characteristics of the bearing under the roller defect and viscous damping. The RMS decreased with viscous damping from 0 Ns/m to 5000 Ns/m. Except for  $f_b + f_c$ , the frequency amplitudes decreased with the increasing viscous damping. The same rules on the fluctuated amplitudes of housing accelerations and for the contact force between the outer ring and housing exist.

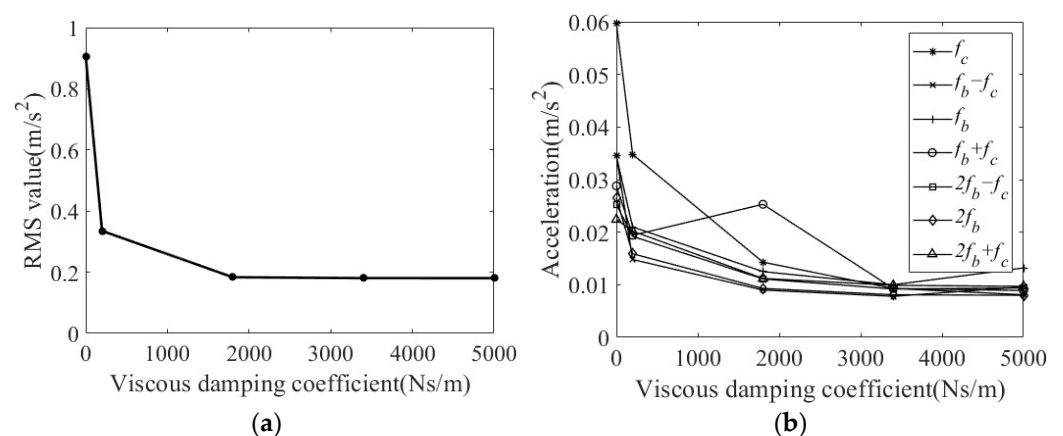


**Figure 25.** Cont.

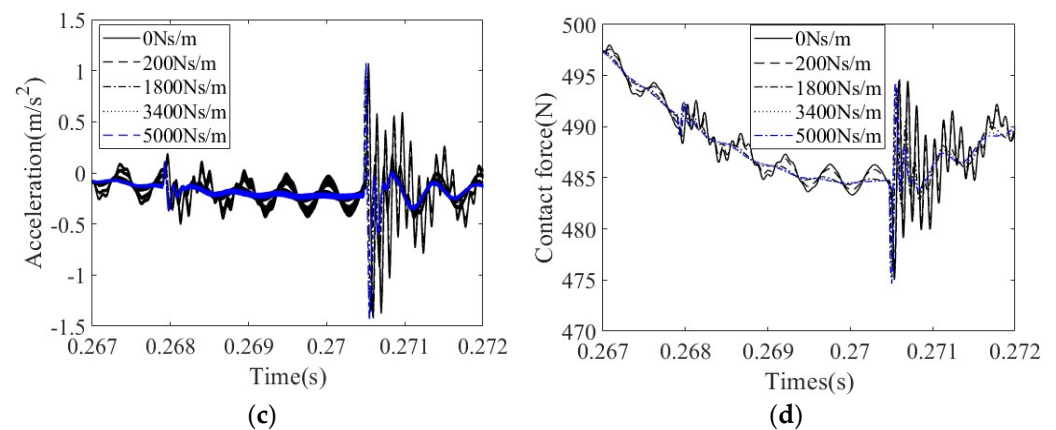


**Figure 25.** The vibration characteristics of the bearing under roller defect and viscous damping: (a) RMS; (b) amplitudes of  $f_c, f_b - f_c, f_b, f_b + f_c, 2f_b - f_c, 2f_b, 2f_b + f_c$ ; (c) housing acceleration signal from 0.267 s to 0.272 s; (d) contact force between outer ring and housing from 0.267 s to 0.272 s.

## 5. Conclusions

In order to investigate the effect of fit clearance on the vibration characteristics of a cylindrical roller bearing with localized defects, a mathematical model for a cylindrical roller bearing was constructed. The fit clearance between the outer ring and housing was considered, and models to study localized defects were built. Then, an experiment was conducted to verify the established bearing model. The effects of fit clearance and its relative parameters on the bearing vibration characteristics were discussed, and the following conclusions are provided:

(1) For the effect of housing stiffness, the sinusoidal fluctuation amplitudes and the RMS of housing acceleration decreased with the housing stiffness from  $1.5 \times 10^7$  N/m to  $2.0 \times 10^8$  N/m. The time interval between the two fluctuation peaks was  $1/f_r$ , and the time lag between the two impacts was related to defect frequencies. The shock time of housing acceleration and contact forces was delayed with the increased housing stiffness for the inner ring defect, but contrary laws exist for the outer ring defect and roller defect. Then, the amplitude of  $f_r$  was the most prominent for the inner ring defect, of which the most remarkable amplitudes were  $f_o$  and  $2f_o$  for outer ring defect, and the most obvious amplitude for the roller defect was  $f_c$ .

(2) For the effect of fit clearance, the RMS increased with fit clearance from 0  $\mu\text{m}$  to 200  $\mu\text{m}$ , but there were no uniform change laws for the amplitudes of defect frequencies. The shock time was delayed with a decreased fit clearance for the outer ring defect and roller defect, but a contrary law for the inner ring defect exists.

(3) For the effect of the friction coefficient, the RMS increases with the friction coefficient from 0.1 to 0.6. However, uniform change rules could not be found in the amplitudes of the defect frequencies. The enlargement fluctuation amplitudes for housing acceleration and contact forces increased with the enhanced friction coefficient.

(4) For the effect of viscous damping, RMS and the amplitudes of defect frequencies decreased with viscous damping from 0 Ns/m to 5000 Ns/m, while the fluctuation amplitudes for housing acceleration and contact forces decreased with an increase in viscous damping.

(5) For the inner ring defect, the phase difference between the defect location and unbalanced force is an important factor. RMS and acceleration fluctuation amplitudes decreased with the phase difference from  $0^\circ$  to  $180^\circ$ , the amplitude of  $f_r$  was found to be remarkable and the phase of contact forces changed with the incremental phase differences. Compared with other defects, the defect location was an important factor for the outer ring defect. The RMS and frequency amplitudes increased with the defect location angle from  $0^\circ$  to  $180^\circ$ . However, a contrary law exists for  $\text{RMS}_y/\text{RMS}$ , acceleration fluctuation amplitudes and contact forces.

(6) From the above analysis, the relative contact forces are found to be affected by the motion of the outer ring. Thus, the dynamic characteristics of the outer ring need to be investigated in detail in future research.

**Author Contributions:** Conceptualization, F.W.; methodology, F.W.; software, X.L. and S.Y.; validation, P.D. and Z.Z.; formal analysis, X.L.; investigation, P.D.; resources, P.D. and Z.Z.; data curation, P.D.; writing—original draft preparation, F.W.; writing—review and editing, S.Y. and F.W.; visualization, L.W.; supervision, S.Y.; project administration, F.W. and L.W. All authors have read and agreed to the published version of the manuscript.

**Funding:** The work described in this paper was fully supported by a grant from the National Science Funds of China (No. 51905001), Start-up Fund of Anhui Polytechnic University (No. 2020YQQ006), Wuhu Science and Technology Projects (No. 2021yf09), Open Research Fund of Anhui Province Key Laboratory of Detection Technology and Energy Saving Devices (JCKJ2021A06).

**Data Availability Statement:** Not applicable.

**Conflicts of Interest:** There are no personal circumstances or interest that may be perceived as inappropriately influencing the representation or interpretation of reported research results in this paper.

## Appendix A

The defect frequencies of cylindrical roller bearing are calculated as [25]:

- (1) rotor frequency

$$f_r = \frac{w_r}{60}$$

- (2) cage frequency

$$f_c = \frac{1}{2} \left( 1 - \frac{d_b}{d_m} \right) f_r$$

- (3) defect frequency for outer ring

$$f_o = n_b f_c$$

- (4) cage passing inner ring frequency

$$f_{ir} = \frac{f_r}{2} \left( 1 + \frac{d_b}{d_m} \right)$$

- (5) defect frequency for roller

$$f_b = \frac{d_m f_r}{2 d_b} \left( 1 - \left( \frac{d_b}{d_m} \right)^2 \right)$$

- (6) defect frequency for inner ring

$$f_i = \frac{f_r}{2} n_b \left( 1 + \frac{d_b}{d_m} \right)$$

## References

1. Sun, J.; Wood, R.; Wang, L.; Care, I.; Powrie, H. Wear monitoring of bearing steel using electrostatic and acoustic emission techniques. *Wear* **2005**, *259*, 1482–1489. [[CrossRef](#)]
2. Sadeghi, F.; Jalalahmadi, B.; Slack, T.S.; Raje, N.; Arakere, N.K. A Review of Rolling Contact Fatigue. *J. Tribol.* **2009**, *131*, 041403. [[CrossRef](#)]
3. Tandon, N.; Choudhury, A. A review of vibration and acoustic measurement methods for the detection of defects in rolling element bearings. *Tribol. Int.* **1999**, *32*, 469–480. [[CrossRef](#)]
4. Shao, Y.; Liu, J.; Ye, J. A new method to model a localized surface defect in a cylindrical roller-bearing dynamic simulation. *Proc. Inst. Mech. Eng. Part J J. Eng. Tribol.* **2013**, *228*, 140–159. [[CrossRef](#)]
5. Wang, F.; Jing, M.; Yi, J.; Dong, G.; Liu, H.; Ji, B. Dynamic modelling for vibration analysis of a cylindrical roller bearing due to localized defects on raceways. *Proc. Inst. Mech. Eng. Part K J. Multi-Body Dyn.* **2014**, *229*, 39–64. [[CrossRef](#)]

6. Liu, J.; Shao, Y. A numerical investigation of effects of defect edge discontinuities on contact forces and vibrations for a defective roller bearing. *Proc. Inst. Mech. Eng. Part K J. Multi-Body Dyn.* **2016**, *230*, 387–400. [[CrossRef](#)]
7. Liu, J.; Shi, Z.; Shao, Y. An analytical model to predict vibrations of a cylindrical roller bearing with a localized surface defect. *Nonlinear Dyn.* **2017**, *89*, 2085–2102. [[CrossRef](#)]
8. Liu, J. A dynamic modelling method of a rotor-roller bearing-housing system with a localized fault including the additional excitation zone. *J. Sound Vib.* **2019**, *469*, 115144. [[CrossRef](#)]
9. Liu, J.; Wang, L. Dynamic modelling of combination imperfections of a cylindrical roller bearing. *Eng. Fail. Anal.* **2022**, *135*. [[CrossRef](#)]
10. Liu, J.; Wang, L.; Shi, Z. Dynamic modelling of the defect extension and appearance in a cylindrical roller bearing. *Mech. Syst. Signal Process.* **2022**, *173*, 109040. [[CrossRef](#)]
11. Patel, U.A.; Upadhyay, S.H. Theoretical model to predict the effect of localized defect on dynamic behavior of cylindrical roller bearing at inner race and outer race. *Proc. Inst. Mech. Eng. Part K J. Multi-Body Dyn.* **2014**, *228*, 152–171. [[CrossRef](#)]
12. Patel, U.A.; Upadhyay, S.H. An analytical model (7 D.O.F.) for the prediction of the vibration response of cylindrical roller element bearings due to a combined localized defect. *Proc. Inst. Mech. Eng. Part K J. Multi-Body Dyn.* **2015**, *229*, 383–406. [[CrossRef](#)]
13. Liu, Y.; Zhu, Y.; Yan, K.; Wang, F.; Hong, J. A novel method to model effects of natural defect on roller bearing. *Tribol. Int.* **2018**, *122*, 169–178. [[CrossRef](#)]
14. Tang, H.; Liu, H.; Zhao, Y.; Tian, G.; Xu, Z. Analysis of mechanics around a localized surface defect of cylindrical roller bearing. *Proc. Inst. Mech. Eng. Part K J. Multi-Body Dyn.* **2018**, *233*, 391–403. [[CrossRef](#)]
15. Patel, S.P.; Upadhyay, S.H. Nonlinear analysis of cylindrical roller bearing under the influence of defect on individual and coupled inner-outer race. *Proc. Inst. Mech. Eng. Part K J. Multi-Body Dyn.* **2018**, *233*, 404–428. [[CrossRef](#)]
16. Patel, S.P.; Upadhyay, S.H. Influence of roller defect and coupled roller-inner-outer race defects on the performance of cylindrical roller bearing. *Proc. Inst. Mech. Eng. Part K J. Multi-Body Dyn.* **2019**, *233*, 731–746. [[CrossRef](#)]
17. Patra, P.; Saran, V.H.; Harsha, S.P. Chaotic dynamics of cylindrical roller bearing supported by unbalanced rotor due to localized defects. *J. Vib. Control* **2020**, *26*, 1898–1908. [[CrossRef](#)]
18. Niu, L.; Cao, H.; Hou, H.; Wu, B.; Lan, Y.; Xiong, X. Experimental observations and dynamic modeling of vibration characteristics of a cylindrical roller bearing with roller defects. *Mech. Syst. Signal Process.* **2019**, *138*, 106553. [[CrossRef](#)]
19. Cao, H.; Su, S.; Jing, X.; Li, D. Vibration mechanism analysis for cylindrical roller bearings with single/multi defects and compound faults. *Mech. Syst. Signal Process.* **2020**, *144*, 106903. [[CrossRef](#)]
20. Su, S.; Cao, H.; Zhang, Y. Dynamic modeling and characteristics analysis of cylindrical roller bearing with the surface texture on raceways. *Mech. Syst. Signal Process.* **2021**, *158*, 107709. [[CrossRef](#)]
21. Xu, H.; He, D.; Ma, H.; Yu, K.; Zhao, X.; Yang, Y. A method for calculating radial time-varying stiffness of flexible cylindrical roller bearings with localized defects. *Eng. Fail. Anal.* **2021**, *128*, 105590. [[CrossRef](#)]
22. Chen, G.; Qu, M. Modeling and analysis of fit clearance between rolling bearing outer ring and housing. *J. Sound Vib.* **2018**, *438*, 419–440. [[CrossRef](#)]
23. Shi, H.; Li, Y.; Bai, X.; Wang, Z.; Zou, D.; Bao, Z.; Wang, Z. Investigation of the orbit-spinning behaviors of the outer ring in a full ceramic ball bearing-steel pedestal system in wide temperature ranges. *Mech. Syst. Signal Process.* **2020**, *149*, 107317. [[CrossRef](#)]
24. Liu, J.; Shao, Y.; Lim, T.C. Impulse vibration transmissibility characteristics in the presence of localized surface defects in deep groove ball bearing systems. *Proc. Inst. Mech. Eng. Part K J. Multi-Body Dyn.* **2013**, *228*, 62–81. [[CrossRef](#)]
25. Harris, T.A.; Kotzalas, M.N. *Advanced Concepts of Bearing Technology*, 2nd ed.; John Wiley & Sons, Inc.: New York, NY, USA, 2006.
26. Gupta, P.K. *Advanced Dynamics of Rolling Element*; Springer-Verlag New York Inc.: New York, NY, USA, 1984.
27. Shi, H.T.; Liu, Z.M.; Bai, X.T.; Hui, M. Crack location recognition method for full ceramic bearing outer ring. *Acta Aeronaut. Astronaut. Sin.* **2021**, *42*. Available online: <http://hkxb.buaa.edu.cn/EN/10.7527/S1000-6893.2021.25481> (accessed on 22 April 2022).